Eur. Phys. J. D **31**, 291–299 (2004)
DOI: 10.1140/epjd/e2004-00139-6

THE EUROPEAN PHYSICAL JOURNAL D

Formation of cold bialkali dimers on helium nanodroplets

M. Mudrich[1,2], O. Bünermann[3], F. Stienkemeier[3], O. Dulieu[2], and M. Weidemüller[1,a]

[1] Physikalisches Institut, Universität Freiburg, 79104 Freiburg, Germany
[2] Laboratoire Aimé Cotton, CNRS, Campus d'Orsay, 91405 Orsay Cedex, France
[3] Fakultät für Physik, Universität Bielefeld, 33615 Bielefeld, Germany

Received 1st July 2004
Published online 26 October 2004

Abstract. Cold alkali diatomic molecules (LiCs, NaCs) in the lowest vibrational state of the electronic triplet ground state are formed on superfluid helium nanodroplets. Using photoionization detection the excitation spectra of the $2^3\Pi \leftarrow 1^3\Sigma^+$ transitions are recorded. The splitting of the vibrational structure in the LiCs spectrum, not observed in the NaCs spectrum, is interpreted in terms of molecular fine structure. The spectra are well reproduced by a model based on quantum chemistry potential curves including spin-orbit coupling, in combination with an asymmetric line shape function to account for cluster-induced broadening. Our refined potential curves provide important input data for the photoassociation of ultracold dipolar alkali molecules from atomic quantum gases.

PACS. 36.40.Mr Spectroscopy and geometrical structure of clusters – 34.50.Gb Electronic excitation and ionization of molecules; intermediate molecular states (including lifetimes, state mixing, etc.) – 33.20.-t Molecular spectra

1 Introduction

The formation of cold heteronuclear molecules has gained great interest in the past years, in particular because of their intrinsic electric dipole moment. Experimental and theoretical efforts are motivated by the prospect of investigating interactions in a cold or even quantum degenerate polar gas [1] by manipulating single dipoles for the purpose of implementing quantum information schemes [2] or for testing fundamental physics [3]. The experimental approaches range from a supersonically expanding gas out of a rotating nozzle [4], "billard-like" collisions [5], reactive collisions [6], Stark deceleration [7], phase-space filtering [8], to buffer gas cooling [9], laser cooling [10], photoassociation starting with a mixed sample of ultracold atoms [11,12] or molecule formation in a two-species Bose-Einstein condensate through a Feshbach resonance [13].

As an alternative approach to the formation of cold molecules, the spectroscopy of molecules isolated in the cold environment of helium nanodroplets was reported for the first time in 1992 for SF_6 [14]. Since then, helium nanodroplet isolation (HENDI) has become a well established tool in the field of cluster physics and matrix isolation spectroscopy [15–18]. In particular, aggregation of molecules and complexes on the droplets has lead to unusual isomers [19,20] as well as weakly bound alkali molecules and clusters [21,22]. The formation of cold heteronuclear alkali dimers on helium droplets has been reported for the specific case of NaK only [21], although alkali atoms and alkali oligomers of one species on helium droplets have already been extensively studied [18]. In this paper we report the formation and spectroscopic investigation of dipolar cold alkali dimers (LiCs, NaCs) on helium nanodroplets in the triplet ground state. These heteronuclear alkali dimers are particularly interesting due to their large permanent dipole moments in covalently bound configurations [23].

HENDI relies on several striking properties of the helium droplets: helium clusters reach an equilibrium temperature of ≈380 mK through spontaneous evaporation of helium atoms [24]. Under certain conditions, atoms, small molecules up to complex organic molecules or even very large metal clusters can be efficiently picked up by the droplets [18,25]. The cluster temperature is subsequently transferred to all degrees of freedom of the dopants. Thus, only the lowest rotational states of the molecular vibrational ground-state are populated. Two or more dopant atoms picked up by the helium cluster in multiple cluster-dopant collisions can form dimers, trimers and higher oligomers in the cluster environment [25]. The released binding energy is subsequently dissipated by evaporation of helium atoms. Since the binding energy of covalently bound alkali molecules exceeds by far the one of

[a] e-mail: m.weidemueller@physik.uni-freiburg.de

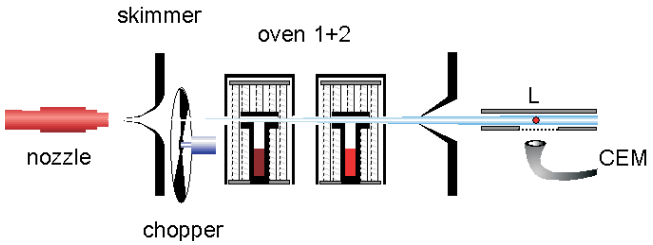

Fig. 1. Schematic representation of the experimental set-up. The beams of the excitation laser and the photoionization laser are coaxially aligned and cross the cluster beam in the perpendicular plane at L. A color version of the figure is available at `www.eurphysj.org`.

van der Waals molecules with parallel spins, the latter favorably stay on the droplets because alkali dimers are, opposed to other dopants, only very weakly bound to the surface of helium droplets. This leads to the enrichment of the cluster beam with triplet dimers with respect to covalently bound ones by up to a factor 10^4 [21].

Spectroscopic shifts induced by the cluster environment are small ($\sim$cm^{-1}) [21]. Therefore the analysis of ro-vibrational spectra provides valuable data to compare with ab initio calculations and previous experimental results. This is particularly appropriate in the case of alkali dimers, since accurate quantum chemistry calculations can be performed. Furthermore, triplet transitions are more difficult to investigate by standard techniques which use the singlet ground state as the initial state. Actually the spectroscopy of LiCs and NaCs is almost unexplored, as it can be checked from the DiRef bibliographic database [26].

We find that the present method of creating a high flux beam of cold cluster sustained heteronuclear alkali dimers supplies a versatile and comparatively simple source for molecular spectroscopy. In particular, this technique is suitable for producing and cooling dipolar molecules.

2 Production of doped helium nanodroplets and detection of cold molecules

The helium cluster beam apparatus is schematically depicted in Figure 1. For a detailed description the reader is referred to reference [27]. Briefly, a beam of helium clusters consisting of 10^4 helium atoms is formed by supersonic expansion behind a 5 μm nozzle at a stagnation pressure of about 60 bar at a nozzle temperature of 21 K (see Fig. 1). The skimmer at the exit of the beam formation chamber has a diameter of 400 μm. In the second chamber, which is pumped by an oil diffusion pump as the first one, the cluster beam passes through two pickup ovens for doping the clusters with a combination of two different alkali atoms. For filling the ovens with the reactive metals rubidium and cesium the oven capsules are immersed in cyclohexane and then, filled up with the solvent, transferred to the vacuum chamber.

Each pickup oven is heated and heat-shielded separately to set an appropriate partial vapor pressure, independently for each metal. The distance between the two oven capsules is 5 cm. A second skimmer 4 mm in diameter is placed at the exit of the pickup chamber. The detection chamber is equipped with two viewports and a channeltron detector in combination with a simple ion optics for detection of photoionized molecules. Alternatively, a detection chamber with two baffles and an imaging system for laser-induced fluorescence (LIF) studies is used. Behind the detection chamber, either a quadrupole mass-spectrometer can be attached for mass-selective photoionization, or a Langmuir-Taylor detector for recording the number of alkali atoms in the helium droplet beam by surface ionization [28]. The latter is used for laser-induced beam depletion measurements (LIBD).

The photoionization (PI) scheme works as follows: the light from a tunable narrow-band titanium:sapphire (Ti:Sa) ring laser (Coherent MBR110) crosses the helium cluster beam at right angle in the horizontal plane and excites the helium cluster sustained molecules in the frequency range 11150–13500 cm^{-1}. The laser frequency is scanned by tuning both the Lyot filter and the etalon. From the width of the LIF signal of the effusive atomic cesium line we infer a spectral resolution in the measured spectra $<$1 cm^{-1}, although the line width of the Ti:Sa laser is expected to be much narrower. The output power is actively stabilized using an acousto-optic modulator. The feedback signal is provided by a photodiode which monitors the laser beam intensity behind the detection chamber. The excited molecules are subsequently ionized by the light of a cw argon-ion (Ar^+) laser (Coherent Innova 90), which is superimposed onto the Ti:Sa laser beam. The Ar^+ laser is operated in multi-line operation with an output power of 8 W and is focused to a beam waist of $\sim$12 μm. The Ti:Sa laser beam is directed to the experiment using a single-mode polarization-maintaining optical fiber. Inside the detection chamber it has a power of 50 mW focused to a waist of 55 μm, which leads to an intensity of 500 W/cm^2. Both excitation and ionization laser beams are overlapped using a beam splitter. Since the beam splitter (a high-reflecting mirror in the frequency range of the Ti:Sa laser) reflects 60% of the Ar^+ laser power, the actual intensity in the focus of the Ar^+ laser is $\sim$500 kW/cm^2. Both foci are adjusted separately in radial and axial directions to optimize the photoionization signal. The ion signal is recorded in lock-in technique using a gated digital counter. The excitation laser is chopped at a frequency of about 500 Hz and the ion counts in the laser on and off periods are subtracted from each other to suppress background counts.

It is important to note that alignment in the horizontal direction is very critical: if the excitation laser is displaced by about 1 mm with respect to the ionization laser towards the cluster source then the cluster beam is depleted by photodesorption before the dopants reach the ionization laser. Instead of detecting a maximum ion count rate on resonance the count rate is minimum as a result of beam depletion. The resulting ionization spectrum will then appear with a negative sign. This observation might be useful in future experiments to study the laser induced desorption dynamics of different dopant atoms or molecules.

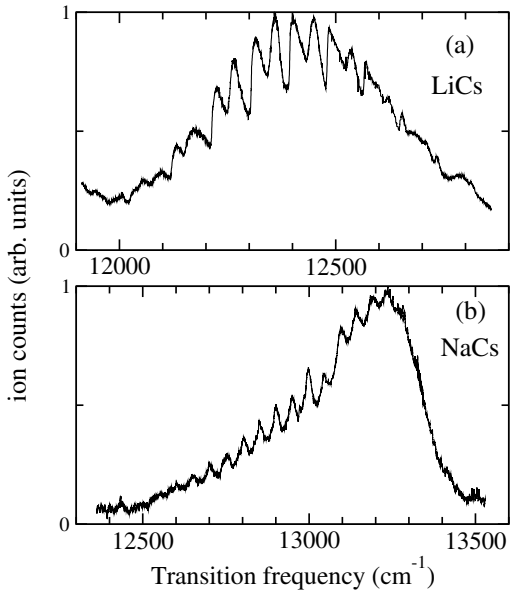

Fig. 2. Excitation spectrum of LiCs (a) and NaCs (b) molecules attached to the helium clusters, recorded using photoionization detection. Ion counts are in arbitrary units.

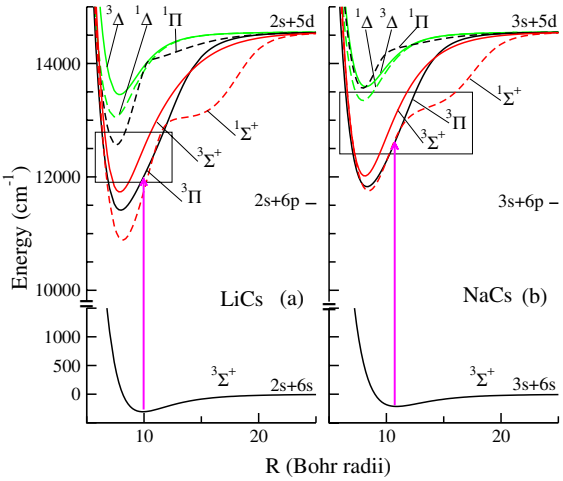

Fig. 3. Triplet (full lines) and singlet (dashed lines) are computed potential curves from reference [31] correlated (a) to the $\mathrm{Li}(2s)+\mathrm{Cs}(5d)$ asymptote, (b) to the $\mathrm{Na}(3s)+\mathrm{Cs}(5d)$ asymptote, photoexcited from the lowest $1^3\Sigma^+$ correlated to $\mathrm{Li}(2s)+\mathrm{Cs}(6s)$ and $\mathrm{Na}(3s)+\mathrm{Cs}(6s)$ respectively (schematized by the vertical arrows). The boxes show the energy range covered in the experiment. The position of the $\mathrm{Li}(2s)+\mathrm{Cs}(6p)$ and $\mathrm{Na}(3s)+\mathrm{Cs}(6p)$ limits is also indicated. A color version of the figure is available at `www.eurphysj.org`.

3 Photoionization spectroscopy of LiCs and NaCs

3.1 Photoionization spectra

In order to record excitation spectra of LiCs or NaCs both the helium cluster source parameters and the laser overlap with the cluster beam are adjusted to optimize the PI signal of the Cs monomer structure, as outlined in [29]. Then, the second oven capsule filled with Li or Na is heated to a temperature at which the probability is expected to be highest that a helium cluster picks up one dopant atom. With the current oven design this condition is fulfilled for a partial vapor pressure of the dopant gas of $\sim 5 \times 10^{-4}$ mbar. Once the PI signal of LiCs and NaCs is found, both Cs and Li/Na oven temperatures are varied to maximize the PI count rate. The optimum oven temperatures are: Cs – 358 K; Li – 698 K; Na – 485 K. The resulting PI spectra of LiCs and NaCs are depicted in Figures 2a and 2b, respectively. Besides Li and Na, Rb is also used as the second dopant atom. Although the characteristic monomer spectra are observed both for Cs and Rb at Rb oven temperatures up to 773 K, no indications for the excitation of RbCs dimers are observed in the spectral range 11500–13500 cm^{-1}. This observation is somewhat surprising given the fact that our model calculations based on computed potential curves of reference [30] predict two vibrational series ($3^3\Sigma^+(6s+5p) \leftarrow 1^3\Sigma^+$ and $2^3\Pi(6s+5p) \leftarrow 1^3\Sigma^+$) in this spectral range.

When recording the spectra, it is carefully checked that the dependence of the signal amplitude on excitation laser intensity is linear, e.g. the transitions are not saturated. The LiCs spectrum is additionally recorded using both LIF and LIBD as detection methods. The resulting spectra are identical to the PI spectrum, however the signal to noise ratio attainable with PI detection exceeds by far the one of LIF and LIBD detection. In order to rule out any perturbations of the spectrum due to excitation of Cs, Cs_2 or any contaminating particle, mass spectra are recorded at various excitation frequencies in the range of the LiCs spectrum. The latter display a strong peak at the mass of LiCs and a small contribution at the mass of Cs, which most probably stems from fragmentation of LiCs into atomic Li and Cs during ionization. The PI spectrum of NaCs, however, is neither cross-checked by different detection methods nor by mass spectra. Since the source parameters are chosen nearly identical to the ones for detecting LiCs, no perturbations of the spectrum are expected. We shall see later on that this assumption is not correct and a contribution of Cs_2 to the observed spectrum must be included.

The LiCs spectrum displays a progression of clearly resolved peaks of widths between 10 and 50 cm^{-1} in the frequency range 12000–12800 cm^{-1}. At larger frequencies, a second series of peaks with larger spacings is observed but not studied in further detail. In the frequency range 11150–12000 cm^{-1} no structures are observed in the spectrum of LiCs. The spectrum of NaCs is recorded in the entire frequency range accessible by the Ti:Sa laser (11150–13500 cm^{-1}) but an excitation spectrum is observed only in the range 12400–13500 cm^{-1}. The maxima are less pronounced than in the LiCs spectrum and the envelope has an asymmetric shape.

3.2 Assignment of the spectra

The analysis of the spectra is based on quantum chemistry potential curves from Korek et al. [31], which do not include spin-orbit coupling (Fig. 3). The frequency

range in which excitation is observed addresses the excited potential curves correlated to $\mathrm{Li}(2s)+\mathrm{Cs}(5d)$ and $\mathrm{Na}(3s)+\mathrm{Cs}(5d)$ atomic asymptotes, respectively. Note that, in contrast to all the other mixed alkali dimers, these asymptotes lie respectively in between $\mathrm{Li}(2s)+\mathrm{Cs}(6p)$ and $\mathrm{Li}(2p)+\mathrm{Cs}(6s)$, and in between $\mathrm{Na}(3s)+\mathrm{Cs}(6p)$ and $\mathrm{Na}(3p)+\mathrm{Cs}(6s)$. Both sets of curves have a similar behaviour, and only the three deepest curves $3^1\Sigma^+, 2^3\Pi, 3^3\Sigma^+$ are lying in the relevant energy domain. No other curve correlated to another asymptote is found to perturb these sets. The $3^1\Sigma^+$ and the $2^3\Pi$ curves in NaCs have comparable well depths (3671 cm^{-1} and 3145 cm^{-1}, respectively), which will be of importance later on. In the experiment, the transitions are assumed to proceed from the $v''=0$ vibrational level of the lowest $1^3\Sigma^+(ns+6s)$ (once again with $n=2,3$ for LiCs and NaCs, respectively) triplet state, so the $3^1\Sigma^+$ cannot be reached by a electric dipole allowed transition.

The transition between $1^3\Sigma^+(v''=0)$ and a vibrational level v^α of an excited molecular state α is controlled by the square of the electric dipole matrix element $|\langle v^\alpha|\mathbf{D}|v''=0\rangle|^2$, where the symbol $\langle\,\rangle$ holds for the integral over the internuclear distance R. Neither theoretical nor experimental data are available for the R-dependent molecular transition electric dipole moment $\mathbf{D}(R)$, so it is fixed to an arbitrary constant in the following calculations. The matrix elements are then approximated by the overlap integrals $|\langle v^\alpha|v''=0\rangle|^2$, called Franck-Condon factors. The numerical solution of the Schrödinger equation for the radial motion of the atoms is found using the LEVEL program of LeRoy [32] and yields transition energies and vibrational wavefunctions for the $2^3\Pi$ and $3^3\Sigma^+$ states, starting from $1^3\Sigma^+(v''=0)$, and assuming $J=0$ for the rotational state.

In order to assign the observed spectra to transitions between electronic states, the spacings between the observed peaks and the spacings between calculated line positions are compared. The maximum of each peak is obtained from least-squares fits of the experimental data with a sum of Lorentzian functions with variable center positions. The results are depicted in Figure 4 (symbols) and compared with the calculated values (lines). In the case of NaCs (Fig. 4b) the experimental data coincide, within the experimental uncertainty, with the calculated vibrational spacings of the $2^3\Pi$ state. In contrast, the spacings between lines in the experimental LiCs spectrum amount to just half the calculated ones for the $3^3\Pi \leftarrow 1^3\Sigma^+(v''=0)$ transition. Therefore, the peaks are alternately labeled "left" and "right" peaks and their energy positions are plotted in Figure 4a. We conclude that the observed spectra are dominated by the $1^3\Pi \leftarrow 1^3\Sigma^+(v''=0)$ transitions and in the case of LiCs there is an additional line splitting mechanism.

Moreover, it is clear from Figure 3 that no other signal is expected in LiCs below 12000 cm^{-1}, as the bottom of the $2^3\Pi$ well is shifted compared to the $1^3\Sigma^+$ one, and as the only other state lying in this region is a singlet state. Beyond 12800 cm^{-1}, the observed progression (not treated here) is probably associated to the $3^3\Sigma^+$ state. Similar conclusions can be drawn for NaCs: there is no other accessible state below 12400 cm^{-1}, whereas the $3^3\Sigma^+$ vibrational progression should be observable beyond 13500 cm^{-1}.

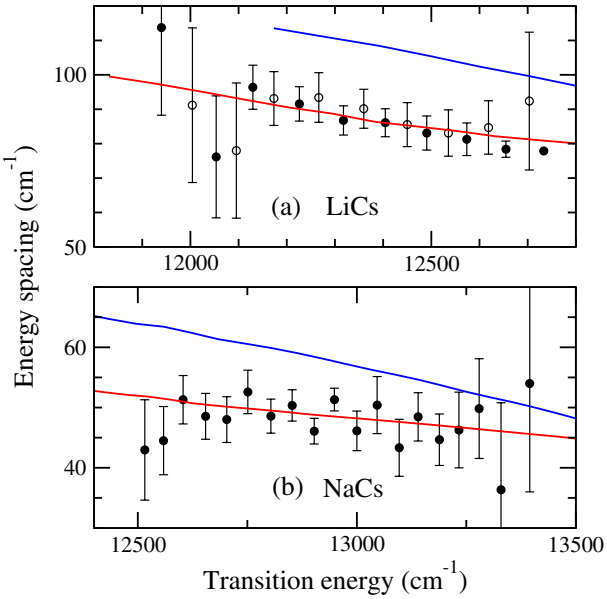

Fig. 4. Experimental line spacings measured for the vibrational spectrum of LiCs (a) and NaCs (b), compared to values computed from the $3^3\Sigma^+$ (full blue line) and $2^3\Pi$ (full red line) potential curves of Figure 3. For LiCs, the measured spacing between "left" (full circles) and "right" (open circles) peaks are displayed. A color version of the figure is available at `www.eurphysj.org`.

3.3 Comparison with ab initio potentials including fine structure

To be more quantitative, the qualitative discussion above has to be completed by the inclusion of the large cesium spin-orbit interaction, which results in a splitting of the $5d$ level into two spectral terms $5^2\mathrm{D}_{3/2}$ and $5^2\mathrm{D}_{5/2}$ separated by $V_{so}=97.584$ cm^{-1} [33]. The potential curves including spin-orbit coupling for the present $ns+5d$ manifold are calculated in a standard perturbative approach (as done for instance in Refs. [34,35] in the $s+p$ case): the spin-orbit Hamiltonian V_{so} is derived within a molecular basis build from atomic wave functions, and involves a constant interaction parameter $A_{5d}=(2/5)V_{so}$. According to standard notations, molecular potential curves with symmetries $\Omega=0^+$, $\Omega=0^-$, $\Omega=1$, $\Omega=2$ and $\Omega=3$ are obtained from the diagonalization of the following Hamiltonians:

$$H(\Omega=3)=\left(V(^3\Delta)+A_{5d}\right) \tag{1}$$

$$H(\Omega=2)=\begin{pmatrix} V(^3\Delta) & A_{5d} & A_{5d}/\sqrt{2} \\ A_{5d} & V(^1\Delta) & -A_{5d}/\sqrt{2} \\ A_{5d}/\sqrt{2} & -A_{5d}/\sqrt{2} & V(^3\Pi)+A_{5d}/2 \end{pmatrix}, \tag{2}$$

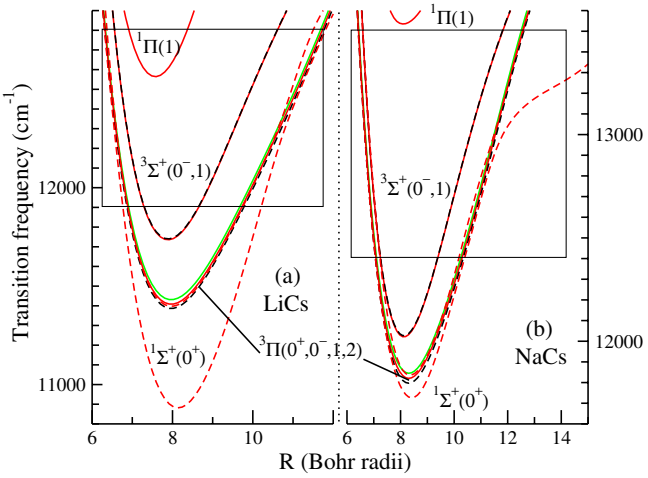

Fig. 5. LiCs (a) and NaCs (b) potential curves including spin-orbit deduced from the diagonalization of the matrices in equations (2–5). The states are labeled with their short range Hund's case a character, and their total symmetry in parenthesis: $\Omega = 2$ (full green curve); $\Omega = 1$ (full red curves); $\Omega = 0^-$ (dashed black curves); $\Omega = 0^+$ (dashed red curves). The frequency range investigated in the experiment is shown with boxes. A color version of the figure is available at `www.eurphysj.org`.

$$H(\Omega=1) = \begin{pmatrix} V(^3\Delta) - A_{5d} & A_{5d}/\sqrt{2} & A_{5d}/\sqrt{2} & 0 \\ A_{5d}/\sqrt{2} & V(^3\Pi) & A_{5d}/2 & \sqrt{3}A_{5d}/2 \\ A_{5d}/\sqrt{2} & A_{5d}/2 & V(^1\Pi) & -\sqrt{3}A_{5d}/2 \\ 0 & \sqrt{3}A_{5d}/2 & -\sqrt{3}A_{5d}/2 & V(^3\Pi) \end{pmatrix}, \quad (3)$$

$$H(\Omega=0^-) = \begin{pmatrix} V(^3\Pi) - A_{5d}/2 & \sqrt{3}A_{5d}/2 \\ \sqrt{3}A_{5d}/2 & V(^3\Sigma^+) \end{pmatrix}, \quad (4)$$

$$H(\Omega=0^+) = \begin{pmatrix} V(^3\Pi) - A_{5d}/2 & \sqrt{3}A_{5d}/2 \\ \sqrt{3}A_{5d}/2 & V(^1\Sigma^+) \end{pmatrix}. \quad (5)$$

The resulting potential curves for $\Omega = 2, 1, 0^-, 0^+$ (we omitted the $\Omega = 3$ state which cannot be excited due to angular momentum conservation) are displayed in Figure 5 in the energy range relevant for the present experiment. The statistical weighting factors for the fine structure components 0^-, 0^+, 1, 2 are 1:1:2:2. In this region, the $^3\Pi$ curve is splitted into three shifted curves with symmetry $\Omega = 2, 1, 0^-$. The analysis of the eigenvectors indeed reveals that the $\Omega = 2, 1, 0^-$ electronic wavefunctions have mostly (more than 98%) $^3\Pi$ character. As illustrated in Figure 6, their vibrational spectrum will be similar to the $^3\Pi$ spectrum shifted in energy, while for a given vibrational level, the FCF's will have the same magnitude up to the statistical weighting factors. In contrast, the $\Omega = 0^+$ state has a significant component on $3^1\Sigma^+$ (Fig. 7), which is larger for NaCs than for LiCs due to the close energy location of the $3^1\Sigma^+$ and $^3\Pi$ states. The

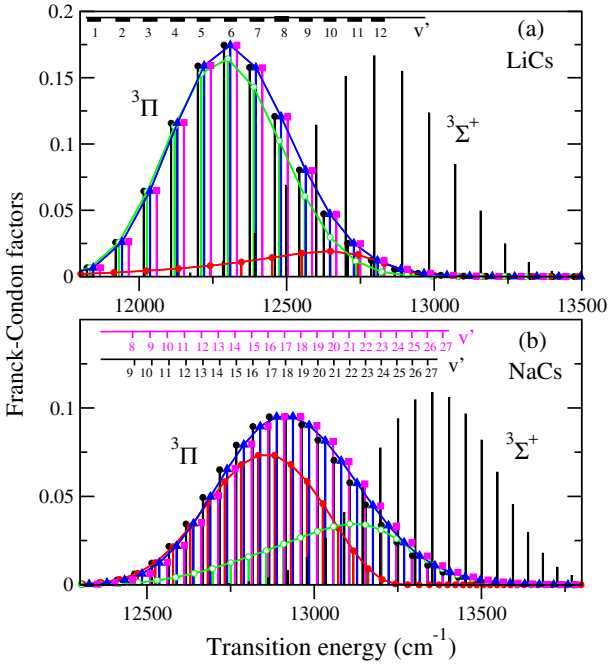

Fig. 6. Computed Franck-Condon factors (FCF) for the transition starting from the lowest $1^3\Sigma^+$ $v'' = 0$ level in LiCs (a) and NaCs (b). Line positions for the following states are represented by vertical bars with symbols: $2^3\Pi(0^-)$ in black with full circles, $3^1\Sigma^+(0^+(n^2\mathrm{S} + 5^2\mathrm{D}_{3/2}))$ in red with full circles, $2^3\Pi(0^+(n^2\mathrm{S} + 5^2\mathrm{D}_{5/2}))$ in green with open circles, $2^3\Pi(1)$ in blue with triangles, $2^3\Pi(2)$ in magenta with squares. The FCF envelope of $\Omega = 1$, $\Omega = 0^+(n^2\mathrm{S} + 5^2\mathrm{D}_{3/2})$, and $\Omega = 0^+(n^2\mathrm{S} + 5^2\mathrm{D}_{5/2})$ are drawn to guide the eye. The FCF envelope for the $3^3\Sigma^+(0^-, 1)$ state is also displayed in black. The quoted vibrational quantum numbers are those computed for the $2^3\Pi$ fine structure components $\Omega = 2, 1, 0^-, 0^+(\mathrm{D}_{5/2})$ in LiCs, and $\Omega = 2, 1, 0^-, 0^+(\mathrm{D}_{3/2})$ in NaCs. The statistical weights of 1:1:2:2 for the states 0^-, 0^+, 1, 2 are omitted. A color version of the figure is available at `www.eurphysj.org`.

R-variation of the $^3\Pi$ component is included in the calculation of the FCF's for the 0^+ states which are both expected to contribute to the signal. Due to its higher mass, the vibrational spectrum of NaCs is more dense than the one of LiCs: Figure 6 shows that the vibrational spacing of the $\Omega = 0^-$ and $\Omega = 2$ series match exactly the fine structure splitting between the two states. The $(v+1)$-lines of $\Omega = 0^-$ and the v-lines of $\Omega = 2$ are found at almost the same transition energies. As discussed later on, this has strong consequences on the shape of the experimental spectra.

Comparing Figures 2 and 6, we find that the observed spectra for both molecules match reasonably well the calculated FCF envelopes for the $2^3\Pi$ fine structure manifolds. In contrast, the calculated FCF envelope for transitions towards the $3^3\Sigma^+$ state, which is predicted to peak inside the frequency range covered by the present work, does not match the experimental findings. In the range 12800–13050 cm^{-1}, the LiCs spectrum displays a series of peaks whose spacings approximately coincide with the calculated ones. However, their amplitudes are suppressed

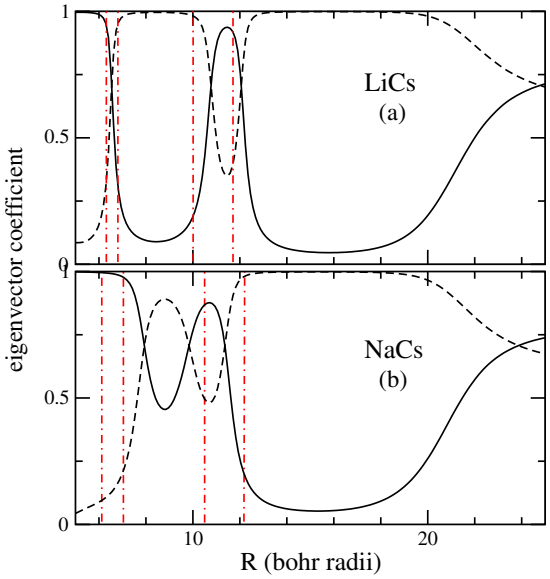

Fig. 7. ($^3\Pi$) component of the $0^+(n^2\mathrm{S} + 5^2\mathrm{D}_{3/2})$ (full line), and $0^+(n^2\mathrm{S} + 5^2\mathrm{D}_{5/2})$ (dashed line) states of LiCs (a) and NaCs (b), resulting from the diagonalization of the perturbative Hamiltonian in equation (5). The vertical bars indicate the range of inner and outer classical turning points of the 0^+ potential curves corresponding to the energy range investigated in the experiment. A color version of the figure is available at `www.eurphysj.org`.

by more than a factor 4 compared to the $2^3\Pi$ series, which may reflect the fact that the $3^3\Sigma^+$ FCF envelope is shifted to larger energies with respect to the calculation.

Several factors could be invoked to explain this discrepancy: (i) the statistical weight of the $3^3\Sigma^+$ state which is two times smaller than the one of the $2^3\Pi$ state, (ii) a possible weak transition probability from the lowest triplet state, (iii) the inaccuracy of the well depth of the state given by the quantum chemistry calculations, (iv) the inaccuracy of the spin-orbit interaction, which is treated here as a perturbation defined by the atomic fine structure. It is hard to predict how these effects cooperate in the final result. Further joint experimental and theoretical investigations are certainly needed to solve this problem. In the following, we will neglect its contribution in the spectra analysis.

3.4 Line shape functions and fit of experimental spectra

In order to compare more quantitatively the model calculations with the experimental data, the calculated FC spectrum has to be convoluted with an appropriate line shape function to account for the interaction of the alkali dimers with the helium clusters. Since the phonon side band extends to higher frequencies with respect to the band origin each resonance is empirically represented by an asymmetric pseudo-Lorentzian function $\mathcal{L}$

Table 1. Fit parameters of the heuristic background functions of the modelled spectra displayed in Figure 8. Parameters o_{bg}, s_{bg} stand for the offset and slope of the linear background function and w_G, ν_G, and A_G for the width, center position and amplitude of the Gaussian background function in the NaCs spectrum. The fit error on the last digit is given in parenthesis.

Parameter	LiCs	NaCs
o_{bg}	5.4(1)	−4.1(3)
s_{bg}/cm	$-4.4(1) \times 10^{-4}$	$3.4(2) \times 10^{-4}$
w_G/cm^{-1}	-	196(4)
ν_G/cm^{-1}	-	13216(2)
A_G	-	0.38(1)

for $(\nu - \nu_v - \nu_g) > 0$,

$$\mathcal{L} = A(\Omega)\, A_v\, w\, (\nu - \nu_v - \nu_g) / \left(4\,(\nu - \nu_v - \nu_g)^2 + w^2\right), \quad (6)$$

and is set to 0 for $(\nu - \nu_v - \nu_g) < 0$. Each line shape function $\mathcal{L}$ of width w is centered at the calculated vibrational energy ν_v for the five relevant fine structure series $\Omega = 2, 1, 0^-, 0^+(\mathrm{D}_{3/2}), 0^+(\mathrm{D}_{5/2})$ and fixed in amplitude to the computed FCF A_v. All functions $\mathcal{L}$ of the same vibrational series are weighted by the same factor $A(\Omega)$ and ν_g accounts for a global shift for all lines with respect to the calculated positions. Alternatively, asymmetric pseudo-Gaussian functions are used but the agreement with the experimental peak profiles is poorer. Using a similar model, the fitted transition frequencies were found to reproduce gas-phase vibronic origins up to an overall shift of $5 \pm 1\,\mathrm{cm}^{-1}$ for the case of Na_2 [21]. In addition, a linear background function $\mathcal{F}_{bg} = s_{bg}\,\nu + o_{bg}$ is added. In the case of NaCs, a Gaussian function $\mathcal{G} = A_G \exp\left(-2\,(\nu - \nu_G)^2 / w_G^2\right)$ of amplitude A_G, width w_G, and centered at ν_G is included empirically in order to account for a Cs_2 absorption peak in that region[1]. The approach of heuristically modelling the slowly varying structures in the spectra by linear and Gaussian functions is similar to applying a filter to the data that extracts quickly varying components.

The sum of all line shape functions and background functions is fitted to the experimental data where the free fit parameters are ν_g, $A(\Omega)$, w, s_{bg}, o_{bg}, and in the case of NaCs, A_G, ν_G and w_G. Alternatively, the numerator $(\nu - \nu_v - \nu_g)$ in equation (6) is raised to the power p to allow for a variable steepness of the rising edge of $\mathcal{L}$. However, the value of p resulting from the fit of the LiCs spectrum is consistent with 1.0 and is held fixed when fitting the spectra.

The model curves resulting from the least squares fits are depicted in Figure 8. The corresponding parameters are listed in Tables 1 and 2. The numbers in brackets

[1] Calculations based on ab initio potential curves [36] reveals the transition $2^3\Sigma_g^+ \leftarrow 1^3\Sigma_u^+$ of Cs_2 lying in this spectral region. Since the uncertainty in the absolute position of the calculated FC profiles appears to be on the order of 100 cm^{-1} [29], the given parameters ν_G and w_G are fitted as well.

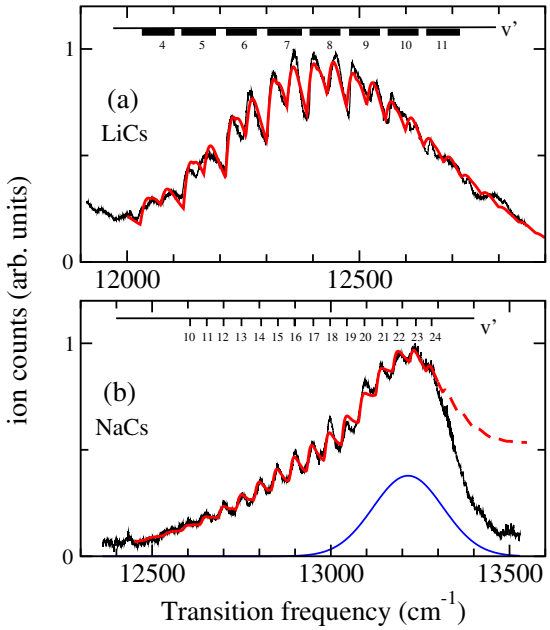

Fig. 8. Experimental spectrum for LiCs (a) and NaCs (b) of Figure 2 (black lines), compared with the best fit obtained according to the procedure described in the text (red line). For NaCs, a Gaussian function (blue line) simulates the influence of an unresolved vibrational Cs_2 band. Since the falling edge on the high-frequency side of the spectrum is dominated by the unresolved Cs_2 background signal it is disregarded in the fit as indicated by the dotted line. The positions of the vibrational levels v' quoted in Figure 6 are reported here, taking into account the global shift ν_g. The v' numbers for NaCs are defined with an uncertainty of about one unit (see text). A color version of the figure is available at `www.eurphysj.org`.

Table 2. Fit parameters of the modelled LiCs and NaCs spectra of Figure 8. $A(\Omega)$ denote the amplitudes of different vibrational series and w is the width of the pseudo-Lorentzian line shape function. All lines are shifted by the global frequency offset ν_g. The amplitudes $A(\Omega)$ for NaCs printed in italic have large systematic uncertainties and cannot be considered as significant.

Parameter	LiCs	NaCs
$A(0^-(D_{3/2}))$	8.9(1)	*2.6(9)*
$A(0^+(D_{3/2}))$	0.0	*0.0*
$A(0^+(D_{5/2}))$	0.0	*3.3(9)*
$A(1(D_{3/2}))$	1.8(2)	*0.0*
$A(2(D_{3/2}))$	7.0(2)	*2.7(9)*
w/cm^{-1}	39.0(9)	29.3(4)
ν_g/cm^{-1}	12.7(2)	20.7(4)

indicate the fit errors to the last significant digit for the given particular set of fit parameters. As seen in Figure 8, it is possible to find for both molecules a set of parameters for $\mathcal{L}$, $\mathcal{F}_{bg}$, and $\mathcal{G}$, which satisfactorily reproduce the experimental spectra. This validates our main hypothesis about the importance of the fine structure components of the $2^3\Pi$ state.

Since the line shape functions $\mathcal{L}$ overestimate the amplitudes of the outer wings on the high frequency side of each vibrational line and add up at the right side of the spectrum the additional linear offset function $\mathcal{F}$ has negative slope s_{bg} to compensate this artefact in the case of LiCs. The NaCs spectrum, however, is fitted only in the range of the rising edge of the envelope of the spectrum (solid line in Fig. 8b), which leads to a positive slope of the background line. Thus, the linear functions $\mathcal{F}$ do not reflect a physical background but rather compensate imperfections in the model assumptions. It is checked, however, that the addition of $\mathcal{F}$ with values s_{bg} from Table 1 alters the position of the maximum of each calculated vibrational line by only $\sim$0.05 cm^{-1}, which is negligible given the experimental precision.

Depending on the choice of the initial value of the global shift parameter ν_g, the fit converges to different values of the fit parameters. For LiCs, the minimum of the χ^2 value is very pronounced and neighboring local minima are found for ν_g shifted by the vibrational interval ($\sim$86 cm^{-1}) to the left or to the right. We can therefore define the vibrational numbering of the series with good confidence, in particular since ν_g remains well below the vibrational interval. In contrast, for NaCs, neighboring local χ^2-minima are found for ν_g shifted by only a few cm^{-1} to the left or to the right with respect to the global minimum. In these cases the amplitudes $A(\Omega)$ are concentrated in different Ω-components. Since the global χ^2-minimum is not very pronounced, the vibrational numbering and therefore ν_g is uncertain by at least one vibrational spacing.

These results emphasizes the quality of the potential curves used here, as they allow to predict the transition energy from the $v = 0$ of the lowest $^3\Sigma^+$ state towards the $2^3\Pi$ vibrational series, with an accuracy of the order of one vibrational spacing for NaCs, or even better for LiCs.

As far as the relative amplitudes $A(\Omega)$ are concerned, no quantitative conclusion can be drawn other than the fact that at least two Ω-components have negligible amplitudes. In LiCs, both $A(0^+)$ amplitudes are found negligible, while the fitted amplitudes for $\Omega = 0^-, 2$ are unambiguously found larger than $A(\Omega = 1)$. According to this model, the double peak structure of the LiCs spectrum reflects the contribution of the $\Omega = 0^-, 2$ components. Such a hierarchy is unexpected since all considered states have mostly a $^3\Pi$ character so they should have comparable excitation probabilities. Moreover the statistical weight of the $\Omega = 1, 2$ components should be twice the one for $\Omega = 0^-_g$. However, due to the width w of the phonon sideband, the vibrational lines strongly overlap each other, which may result in correlations among the fitted amplitudes. Also, our model for the molecular fine structure does not include the R-variation of the molecular spin-orbit coupling which should be computed with quantum chemistry approaches. The relative position of the $2^3\Pi$ fine structure components could well be inaccurate.

As mentioned earlier, in NaCs, the vibrational structure of the molecular fine structure states is calculated

to be more dense than in LiCs (see Fig. 6), in particular the vibrational spacing within the $\Omega = 2$ and $\Omega = 0^-$ states matches the energy spacing between these two components. This explains why the observed lines have no structure as all vibrational lines then collapse into a single profile. In the fit presented in Table 2, the $\Omega = 1$ component is found negligible, while the $\Omega = 0^+(\mathrm{D}_{5/2})$, which is close in energy to the $^3\Pi$ manifold, has now a fairly large weight. This hierarchy actually changes from the absolute χ^2-minimum to the neighboring local minima, so that the results for the relative Ω amplitudes are even less conclusive than for LiCs.

It is interesting to note that the phonon sideband width w strongly depends on the molecule. The corresponding full widths at half maximum (FWHM) amount to around 68 cm^{-1} and 50 cm^{-1} for LiCs and NaCs, respectively. Similarly, Higgins et al. [21] obtained in Na_2 different FWHM values depending on the electronic state of the molecule (around 28 cm^{-1} and 130 cm^{-1} for the transitions $1^1\Sigma_u^+ \leftarrow 1^1\Sigma_g^+$ and $1^3\Sigma_g^+ \leftarrow 1^3\Sigma_u^+$, respectively) and about 30 cm^{-1} for the transition $2^3\Sigma^+ \leftarrow 1^3\Sigma^+$ of NaK. This indicates stronger coupling to the helium surface of LiCs and NaCs than the lighter alkali dimers.

4 Conclusion

We demonstrate efficient formation of heteronuclear alkali dimers (LiCs, NaCs) on helium nanodroplets after successive pickup of different species alkali atoms. Different detection methods including mass selective photoionization are used for recording excitation spectra. In order to well reproduce the spectra available quantum chemistry potential curves [31] are modified to include fine structure in a perturbative approach. A pseudo-Lorentzian line shape function is found to be the best model for the line broadening induced by the interaction with the helium environment. From least-squares fits we find the assignment of vibrational lines and a global frequency shift of 12.7 (20.7) cm^{-1} between experimental LiCs (NaCs) data and the calculated Franck-Condon spectra.

This demonstrates that even spectroscopy that is limited in resolution by the alkali-helium surface interactions puts strong constraints on the calculated potential curves. The latter are found accurate enough to infer the value of the transition energies from the lowest level of the initial $^3\Sigma^+$ state towards the vibrational series of the $2^3\Pi$ fine structure manifold with an accuracy of the order, or better than, one vibrational spacing. Thus the assignment of vibrational lines of the fine structure states can be accurately predicted for LiCs and for NaCs up to about one vibrational energy spacing. Our spectroscopic data actually provides the first results on the triplet transition system in LiCs and NaCs, whose spectroscopy is almost unexplored yet. The comparison to high-resolution gas-phase measurements, which are currently under way [37], will give further insight into the physics of alkali molecules attached to helium nanodroplets. In view of recent developments in the field of ultracold quantum gases [11,13], spectroscopy of bialkali molecules on helium nanodroplets can provide important spectroscopic input data for the formation of ultracold molecular quantum gases through photoassociation. High-resolution rotationally resolved spectra are in principle feasible with HENDI as well by probing molecules which are desorbed from the droplets [38].

In future experiments, the demonstrated scheme could also be utilized for decelerating and trapping cold molecules. The flux of molecule doped helium nanodroplets is estimated to be on the order of $10^{10}\,\mathrm{s}^{-1}$, which corresponds to a density of $10^8\,\mathrm{cm}^{-3}$. Deceleration of the doped nanodroplets could be achieved by subsequent ionization of the nanodroplets and stopping using electrostatic fields [39]. Besides the ionization by electron impact or by photoionization [40] it is also conceivable to create charged doped helium nanodroplets by electron capture [41] or by directly doping ions [42]. Subsequent trapping in an ion trap for doped helium clusters could be realized in analogy to e.g. trapping metal clusters in a Penning trap [43]. Finally, photodesorption of the cold molecules from the helium nanodroplets and trapping in an electrostatic [7] or magnetic trap [44] is a further option. A suitable electronic transition towards coupled singlet and triplet excited molecular states may also be used to transfer these triplet molecules into the singlet manifold, where they exhibit strong permanent dipole moments.

We acknowledge fruitful discussions with Eberhard Tiemann. This work was supported by the Deutsche Forschungsgemeinschaft in the framework of the SPP1116 (with special thanks to the coordinator Martin Wilkens for the unbureaucratic handling of the administration) and by the European Research and Training Network COMOL (contract HPRN-CT-2002-00290).

References

1. M.A. Baranov et al., Phys. Rev. A **66**, 013606 (2002)
2. D. DeMille, Phys. Rev. Lett. **88**, 067901 (2002)
3. M.G. Kozlov, L.N. Labzowsky, J. Phys. B **28**, 1933 (1995)
4. B.S. Zhao et al., Rev. Sci. Inst. **75**, 146 (2004)
5. M.S. Elioff et al., Science **302**, 1940 (2003)
6. U. Wiedermann, Ph.D. thesis, Universität Bielefeld (1992)
7. H.L. Bethlem et al., Nature **406**, 491 (2000)
8. S.A. Rangwala et al., Phys. Rev. A **67**, 043406 (2004)
9. J.D. Weinstein et al., Nature **395**, 148 (1998)
10. M.D. Di Rosa et al., Book of abstracts of the *Joint Harvard/MIT Center for Ultracold Atoms Worshop on Ultracold Polar Molecules: Formation and Collisions*, January 8-10, 2004
11. A.J. Kerman et al., Phys. Rev. Lett. **92**, 033004 (2004)
12. M.W. Mancini et al., Phys. Rev. Lett. **92**, 133203 (2004)
13. A. Simoni et al., Phys. Rev. Lett. **90**, 163202 (2003)
14. S. Goyal et al., Phys. Rev. Lett. **69**, 933 (1992)
15. J.A. Northby, J. Chem. Phys. **115**, 10065 (2001)
16. C. Callegari et al., J. Chem. Phys. **115**, 10090 (2001)
17. F. Dalfovo et al., J. Chem. Phys. **115**, 10078 (2001)
18. F. Stienkemeier et al., J. Chem. Phys. **115**, 10119 (2001)
19. K. Nauta, R.E. Miller, Science **283**, 1895 (1999)

20. K. Nauta, R.E. Miller, Science **287**, 293 (2000)
21. J. Higgins et al., J. Phys. Chem. A **102**, 4952 (1998)
22. C.P. Schulz et al., Phys. Rev. Lett. **92**, 013401 (2004)
23. G. Igel-Mann et al., J. Chem. Phys. **84**, 5007 (1986)
24. M. Hartmann et al., Phys. Rev. Lett. **75**, 1566 (1995)
25. M. Lewerenz et al., J. Chem. Phys. **102**, 8191 (1995)
26. P.F. Bernath, S. McLeod, J. Mol. Spectrosc. **207**, 287 (2001); `http://diref.uwaterloo.ca/`
27. F. Stienkemeier et al., Eur. Phys. J. D **9**, 313 (1999)
28. F. Stienkemeier et al., Rev. Sci. Instr. **71**, 3480 (2000)
29. O. Bünermann et al., J. Chem. Phys. (2004, in press)
30. A.R. Allouche et al., J. Phys. B **33**, 2307 (2000)
31. M. Korek et al., Can. J. Phys. **78**, 977 (2000)
32. R.J. LeRoy, *Chemical Physics Research Report* (University of Waterloo, CP-555, 1995)
33. K.-H. Weber, C.J. Sansonetti, Phys. Rev. A **35**, 4650 (1987)
34. A. Fioretti et al., Eur. Phys. J. D **5**, 389 (1999)
35. J. Reho et al., J. Chem. Phys. **113**, 9694 (2000)
36. N. Spies, Ph.D. thesis, Universität Kaiserslautern (1989)
37. E. Tiemann, private communication (2004); O. Docenko et al., Phys. Rev. A **69**, 042503 (2004)
38. F. Stienkemeier et al., Phys. Rev. Lett. **74**, 3592 (1995)
39. T. Jiang, J.A. Northby, Phys. Rev. Lett. **68**, 2620 (1992)
40. R. Fröchtenicht et al., J. Chem. Phys. **104**, 2548 (1995)
41. U. Henne, J.P. Toennies, J. Chem. Phys. **108**, 9327 (1998)
42. P. Claas et al., Rev. Sci. Instrum. **74**, 4071 (2003)
43. S. Becker et al., Rev. Sci. Instrum. **66**, 4902 (1995)
44. N. Vanhaecke et al., Phys. Rev. Lett. **89**, 063001 (2002)